

Self-locked broadband Raman-electro-optic microcomb

Received: 21 July 2024

Accepted: 15 May 2025

Published online: 24 May 2025



Shuai Wan^{1,2,3,5}, Pi-Yu Wang^{1,2,3,5}, Ming Li^{1,2,3,5}, Rui Ma⁴, Rui Niu^{1,2,3}, Fang-Wen Sun^{1,2,3}, Fang Bo⁴✉, Guang-Can Guo^{1,2,3} & Chun-Hua Dong^{1,2,3}✉

Optical frequency combs (OFCs), composed of equally spaced frequency lines, are essential for communications, spectroscopy, precision measurement, and fundamental physics research. Recent developments in integrated photonics have advanced chip-scale OFCs, enabling on-chip OFC generation via the Kerr or electro-optic (EO) effect. However, these nonlinear processes can occur simultaneously and are often accompanied by parasitic effects, like Raman scattering, which may impede broadband and low-noise microcomb generation. Here, we harness these interactions to demonstrate a novel OFC, the self-locked Raman-electro-optic (REO) microcomb in a lithium niobate microresonator. By leveraging the collaboration of EO, Kerr and Raman scattering, the REO microcomb spans over 300 nm (~1400 lines) with a 26.03 GHz repetition rate, achieving low-noise operation without external feedback. Our approach points to a direction for improving the performance of microcombs and paves the way for exploring new nonlinear physics, such as new laser locking techniques, through the multi-nonlinear synergy.

Integrated photonics has markedly revolutionized the generation and manipulation of light on a microscale in recent years, heralding a new era in photonic technologies. One of the most transformative developments is the realization of optical frequency combs (OFCs) in on-chip nonlinear microresonators^{1–6}. OFCs, consisting of evenly spaced discrete spectral lines, have emerged as essential tools in modern photonics, profoundly transforming fields like precision timing, spectroscopy, and high-speed communications^{7–14}. Traditional OFCs, generated via mode-locked lasers, require bulky laboratory setups, limiting their practical applications outside laboratory environments^{15–17}. Consequently, substantial efforts have been made to integrate OFCs into compact, chip-scale systems^{18–21}.

Currently, the primary approaches for generating on-chip OFCs are based on the Kerr effect, specifically dissipative Kerr solitons (DKSs), and the electro-optic (EO) effect, known as EO combs. While

DKSs enable ultrafast, passive mode-locking and can facilitate envelope design and spectrum broadening through dispersion engineering, their generation requires precise control⁴. In contrast, EO combs, which have been implemented in lithium niobate (LN) and lithium tantalate (LT) resonators and waveguides, are easier to generate and can be directly locked to microwave frequencies but exhibit limited spectral width and depend heavily on microwave power^{22–26}. Additionally, the generation of OFCs is often accompanied by parasitic nonlinear effects, such as Raman scattering^{27,28}. Raman scattering facilitates nonlinear power transfer from the pump to Stokes lines through inelastic photon-phonon interactions. It has been shown to enhance both the spectral bandwidth and conversion efficiency of OFCs through nonlinear pumping^{29–32}. However, Raman scattering can also introduce additional frequency noise and hinder the generation and expansion of OFCs^{33–36}. To fully leverage the advantages of both

¹Laboratory of Quantum Information, University of Science and Technology of China, Hefei, Anhui, People's Republic of China. ²CAS Center For Excellence in Quantum Information and Quantum Physics, University of Science and Technology of China, Hefei, Anhui, People's Republic of China. ³Hefei National Laboratory, University of Science and Technology of China, Hefei, Anhui, People's Republic of China. ⁴MOE Key Laboratory of Weak-Light Nonlinear Photonics, TEDA Applied Physics Institute and School of Physics, Nankai University, Tianjin, People's Republic of China. ⁵These authors contributed equally: Shuai Wan, Pi-Yu Wang, Ming Li. ✉ e-mail: bofang@nankai.edu.cn; chunhua@ustc.edu.cn

DKSs and EO combs while overcoming their inherent limitations and mitigating parasitic nonlinear effects, exploring the synergy of multiple nonlinear effects is a promising approach. However, the simultaneous occurrence and synergy of multiple nonlinear effects involve complex physical mechanisms, making the achievement of high-performance nonlinear OFCs in a single device a critical unresolved issue.

Here, we introduce a new type of OFC, by collaborating Raman, EO, and Kerr effects in a single LN racetrack microresonator to produce a broadband and flat Raman-electro-optic (REO) microcomb. This novel mechanism, diverging from systems dependent on single nonlinearities, employs Raman scattering and EO modulation to generate diverse EO comb sets, while leveraging four-wave mixing (FWM) to further broaden the spectral width. In particular, comb lines originated from the Raman laser, are self-adaptively phase-locked to the optical and microwave fields without any external electronic feedback loop, ensuring high coherence and fast tunability of the whole microcomb. The resulting broadband REO microcomb, not only showcases an impressive spectral width of 300 nm, but also maintains a precise repetition rate of 26.03 GHz across nearly 1400 comb lines. Moreover, this microcomb features tunable repetition rates and pump laser frequencies, offering precise control of comb characteristics to enhance performance and broaden application scopes.

Results

Schematic of self-locked Raman-electro-optic microcomb

Figure 1 illustrates the configuration of the REO microcomb generation based on a LN racetrack microresonator. Efficient coherent energy transfer between adjacent cavity modes occurs when the microwave modulation frequency aligns with the free spectral range (FSR) of the microresonator. This transfer, induced by the EO effect, sequentially shifts the energy of the pump laser to nearby modes one by one, forming the pure EO comb. While increasing the laser pump power enhances the power of all comb lines, it does not enhance the EO coupling strength. However, significant Kerr nonlinear processes can arise and help to expand the spectral width by delivering photons to different modes via FWM. Meanwhile, as the pump power increases above the Raman threshold, Raman laser can be generated from solely vacuum noise, which further initiates additional EO combs under microwave modulation, as shown in Fig. 1b. However, the frequency of the Raman lasers depends on the mode detuning and dissipation, thus the frequency difference with the pump laser may not be equal to an integer multiple of the microwave frequency. This leads to a difference (δ) in the carrier-envelope offset frequency f_{ceo} between the primary EO comb and the Raman EO comb, as shown in the right inset of Fig. 1b. Moreover, the field intensity in the pump mode is clamped due to the threshold nature of the Raman process, which limits the field intensity

in all comb lines and eventually the total power and bandwidth of the EO comb.

Fortunately, the collaboration of these nonlinearities provides a route to self-adaptively eliminate the δ and merge these combs into a single broader microcomb. The mechanism is organized as follows: (1) Anomalous dispersion in the microresonator enhances FWM, creating overlapping spectral lines between the primary and Raman EO combs. In the overlap region, there are multiple comb lines in a single mode, with frequencies differed by δ ; (2) The Kerr nonlinearity transfers this frequency difference δ to the Raman gain region, producing a sideband around the Raman laser. The frequency of this sideband differs to the pump laser by integer multiples of the microwave frequency; (3) This sideband competes in the Raman scattering process, potentially serving as a seed for frequency locking. Proper tuning of microwave frequency and pump power can reduce δ , leading to the frequency synchronization of the Raman EO comb lines with the primary EO comb and the alignment of the f_{ceo} , as shown in the inset of Fig. 1b. This mechanism exhibits partial similarities to laser injection locking¹⁸. However, unlike external locking approaches, the frequency stabilization here originates from coherent nonlinear interactions within a single device³⁷, mediated by the coupling between the broadened comb spectrum and the Raman gain profile, which collectively enforce phase locking.

Experimental setup and microcomb characterization

The experimental setup is shown in Fig. 2a. The broadband REO microcomb is experimentally demonstrated using an x-cut thin film lithium niobate (TFLN) photonic chip, as shown in Fig. 2b. Figure 2c presents the microscope image of the racetrack microresonator with the FSR of about 26.03 GHz. Detailed information about the device fabrication can be found in the Methods section. The pump laser (Toptica CTL 1550) is amplified and polarization-controlled to match the quasi-TE mode of the on-chip waveguide, and then coupled into the waveguide supporting the fundamental TE mode through a lensed fiber. The transmitted light is collected by another lensed fiber and sent into subsequent characterization instruments. The coupling loss is approximately 6 dB per facet. An RF signal, which matches the FSR of the microresonator, is amplified and applied to drive the on-chip electrode. Figure 2d shows the pumped mode resonates around the wavelength of 1571.04 nm with a loaded Q-factor of 1.1×10^6 . The dispersion of the microresonator around 1571 nm, shown in Fig. 2e, is analyzed using the integrated dispersion formula $D_{int} = \frac{1}{2}D_2\mu^2 + \frac{1}{6}D_3\mu^3 + \dots$, yielding $D_2/2\pi = 3.92$ kHz indicating anomalous and flat dispersion, which is crucial for expanding the spectral width and locking the microcomb.

Figure 2f displays the optical spectra of microcombs under different pump conditions. The comb initiation scheme is the same as the

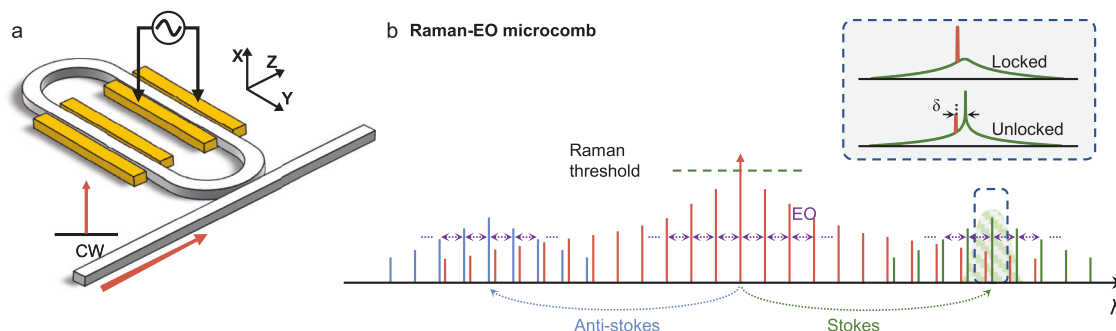


Fig. 1 | Schematic of the hybrid electro-optic comb. **a** The EO comb is generated by coupling a continuous-wave (cw) pump laser into a LN resonator under microwave modulation. **b** Spectrum of the EO comb when the pump laser is above the Raman lasing threshold. The EO combs spread around the pump laser and Raman laser share the same f_{rep} but have different f_{ceo} (unlocked state). With the help of

four-wave mixing (FWM), these two combs expand their bandwidths and overlap. The beating frequency of the two combs in the overlapped modes is transferred to the Raman laser mode and finally locks the Raman lasing frequency being integer multiples of the microwave frequency from the pump frequency (locked state).

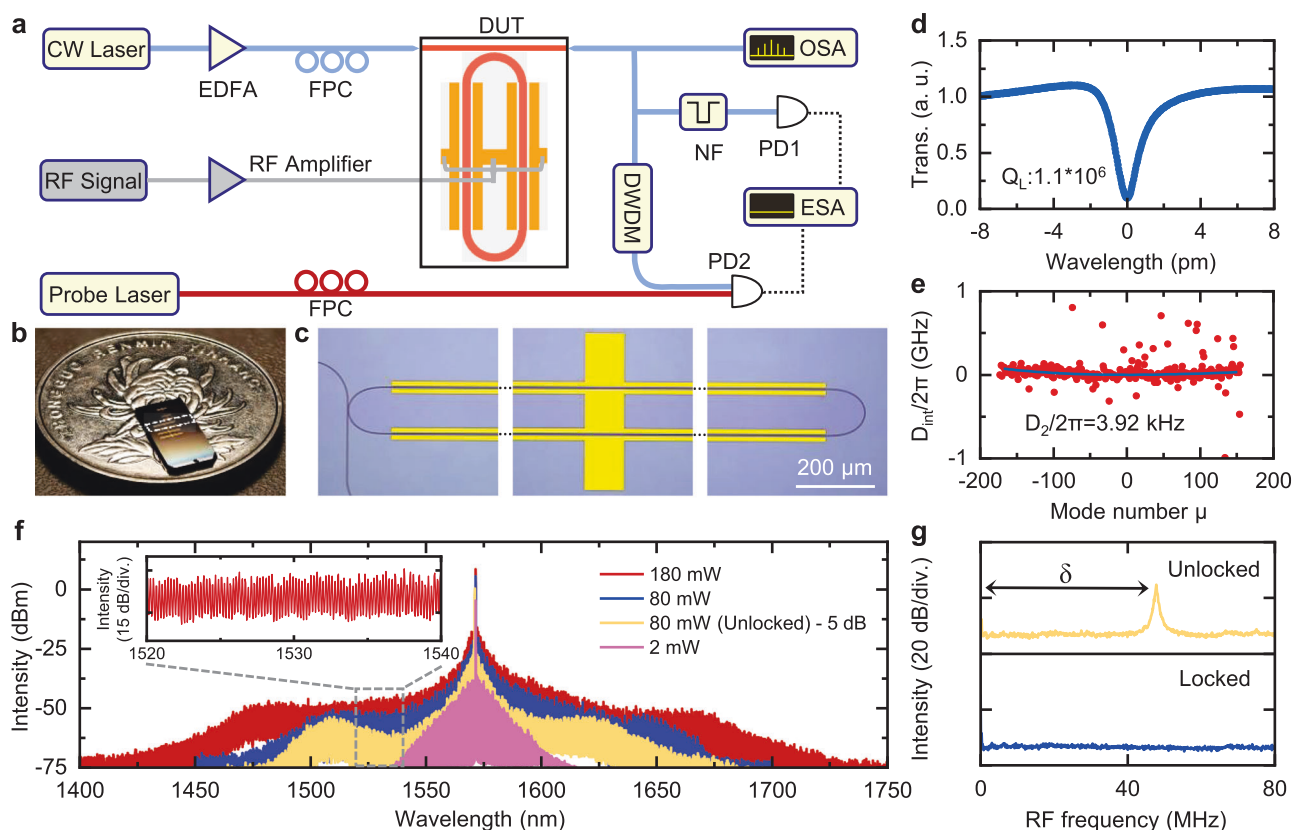


Fig. 2 | Experimental setup and device characterization. **a** Schematic of the experimental setup. EDFA: erbium doped fiber amplifier; FPC: fiber polarization controller; OSA: optical spectrum analyzer; DWD: dense wavelength division multiplexing; NF: notch filter; ESA: electrical spectrum analyzer. **b** Photograph of the thin film lithium niobate (TFLN) photonic chip. **c** The microscope image of the device consisting of a LN racetrack microresonator and electrodes. **d** The transmission spectrum of a typical fundamental TE mode with a fitted loaded Q-factor of 1.1×10^6 . **e** Red dots are the dispersion of the microresonator around 1571 nm

measured by the Mach-Zehnder interferometer (MZI). Blue curve is the fitted curve, with the fitted value of $D_2/2\pi$ being 3.92 kHz. **f** The optical spectra of the hybrid microcomb under different on-chip optical pump power. The driven RF power is 30 dBm. The intensity of the yellow curve for 80mW (Unlocked) is vertically offset by -5 dB to mitigate overlap with other curves. The inset on the upper left corner shows a flat spectrum between 1520 nm and 1540 nm. **g** The RF spectra of the output comb field. The disappearance of the beating frequency indicates the whole output field being in a phase-locked state.

conventional EO combs (see Supplementary Information). At a low on-chip optical pump power of 2 mW, the EO effect predominates, producing a typical EO comb profile with the spectral width of 80 nm with the modulation frequency around 26.03 GHz. When the pump power exceeds the Raman laser threshold, two additional sets of EO combs emerge on both sides of the primary comb due to the combined effects of Raman scattering and FWM, as shown by the yellow curve in Fig. 2f. These comb structures are referred to as the Stokes comb and the anti-Stokes comb. The spectral width of the hybrid comb becomes significantly wider than that of the pure EO comb at low pump power. After filtering out the pump laser, the output comb field is injected to the photodetector (PD) and analyzed by the electrical spectrum analyzer (ESA). A beat signal in the upper panel of the Fig. 2g, indicates a frequency difference δ of about 48 MHz between the primary EO comb line and the Raman EO comb line within the same resonance mode, implying distinct frequency offsets f_{ceo} and preventing treatment as a single phase-locked comb. This beating frequency depends on the pump and microwave driving conditions as well as environment noise. Through adjusting the microwave modulation frequency to reduce the δ , an abrupt disappearance of the beat signal reveals that these combs is merged into a single one (lower panel of the Fig. 2g). The locked REO microcomb shows a broad spectral width and obvious flatness along the wings (blue curve in Fig. 2f), which is consistent with numerical simulations in Supplementary Information. With further increasing optical pump power to 180 mW, more significant Kerr effect can expand the spectral width further to over 300 nm. It is worth noting

that the sideband slope of the REO microcomb in the region around the pump is comparable to that of a conventional EO comb (about 1 dB/nm), while the sideband slope in the flattest region (inset of Fig. 2f) is only about 0.1 dB/nm, which is an order of magnitude smaller.

Locking behavior of the microcomb

To characterize the self-locked state of the REO microcomb and exclude any accidental alignment of the primary and Raman EO combs, we experimentally investigate the locking dynamics by varying the microwave frequency under fixed optical pump power (150 mW) and modulation power (30 dBm). The microwave modulation frequency starts at 26.03 GHz. As the modulation frequency is increased to better match the FSRs near the pumped mode, the spectral width of the entire microcomb broadens progressively, as illustrated in Fig. 3a. Meanwhile, the intensity peak of the comb lines gradually shifts from longer to shorter wavelengths (from Stokes to anti-Stokes comb). This shift is attributed to the anomalous dispersion of the microresonator, where the FSR increases from longer to shorter wavelengths. Figure 3b provides a detailed view of how the spectral intensity distribution varies with the modulation frequency.

Limited by the resolution of the OSA, the details around the overlap region are challenging to discern. Therefore, a probe laser around 1541 nm is employed to detect the comb lines in the overlap region. The probed comb lines near 1541 nm are extracted by filtering other comb lines using dense wavelength division multiplexing

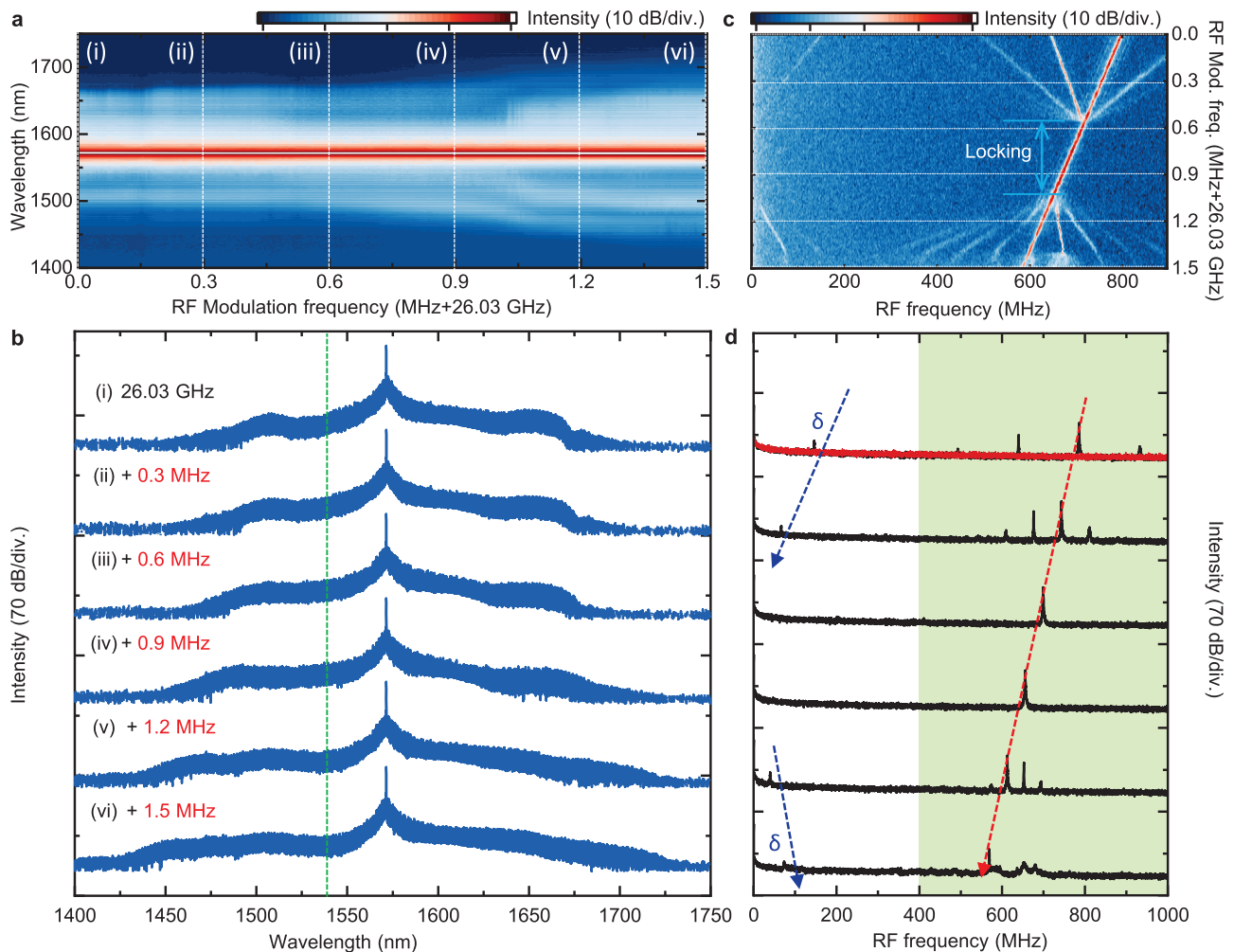


Fig. 3 | Locking behavior of the REO microcomb. a, b The evolution of the optical spectra when scanning the microwave modulation frequencies. The green line shows the position of the probe laser. **c, d** Measured beat note signals between comb lines near the green line and a probe laser at 1541 nm for different microwave

frequencies. The corresponding beat note signals captured by an ESA, showcasing three distinct type of spectra, representing self-locked and unlocked states of the hybrid microcomb.

(DWDM). The corresponding beat signals are displayed in Fig. 3c, d. There are two distinct groups of beat signals in the RF spectra. The lower one, corresponding to the frequency difference δ between comb lines, gradually decreases and disappears with increasing the modulation frequency, and then reappears after hundreds of kHz, as indicated by the blue dashed line in Fig. 3d. The disappeared region corresponds to the locking range, which can also be confirmed by the beat signal of the probe laser with the comb lines in the nearest cavity mode, i.e., another group of beat signals at higher frequency. The central peak of this group of beat signals, marked in red dashed line in Fig. 3d, represents the comb line from the primary comb, and the slope of this red dashed line represents the mode index of the probed mode relative to the pumped mode. The peak spacing equals to the offset difference δ , which scales linearly with the microwave frequency. When the modulation frequency is outside the locking range, both the primary and Raman comb lines coexist within the cavity mode, along with their FWM generated sidebands. Otherwise, there is only one single comb line within the cavity mode. The sudden shift of the beat signals and its dependence on the microwave frequency are clear indicators of the self-locking process. The width of the corresponding locking range can reach 520 kHz, indicating the robustness of the self-locked microcomb against small variations in the pump and microwave fields as well as environment fluctuations. The self-locked microcomb exhibits a flat distribution of comb lines at its wings,

which is attributed to the effect of Raman gain and Kerr effect. Furthermore, the self-locking mechanism also suppresses the linewidth and frequency jitter of the Raman comb, ensuring its alignment with the primary comb (see Supplementary Information), as widely seen in injection locking experiments¹⁸. In this way, the self-locking mechanism transforms the Raman scattering into a crucial nonlinear gain mechanism for broadband EO comb generation.

Indeed, the locking range of the microcomb offers a precise tuning method for fine-tuning f_{rep} across several hundred kHz. To realize extensive tuning of f_{rep} , it is necessary to demonstrate that the microcomb can remain locked under various microwave frequencies that are significantly different. By adjusting the pump laser frequency, the locking range can be changed, as depicted in Fig. 4a. It is observed that the locking range gradually shifts to lower frequency as the pump laser frequency is decreased, due to the diminishing frequency difference between the pump laser and the Raman laser. When the pump laser frequency is excessively high, the detuning between the pump laser and the cavity mode becomes too large, resulting in the decrease of intracavity power. Consequently, the locking range narrows until phase locking becomes unsustainable. Conversely, when the pump laser frequency is too low, the pump laser shifts to the red-detuned side of the cavity mode, causing it to exit the cavity mode. The upper and lower boundaries at different laser frequencies define a locking region, within which the locking range

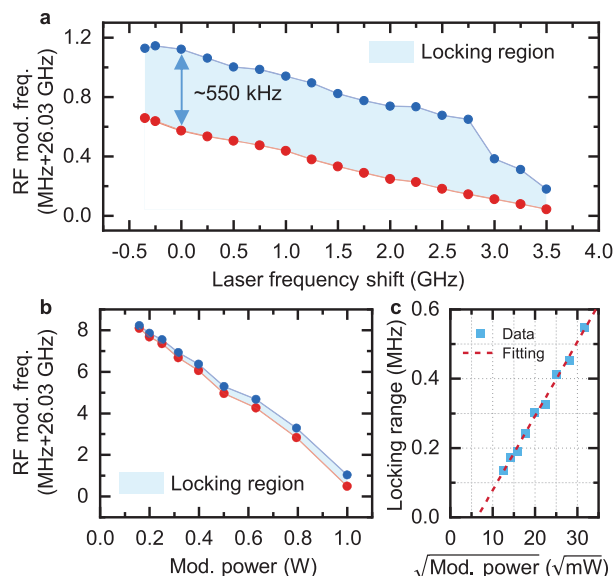


Fig. 4 | Variation of locking range at different modulation frequencies and powers. **a** Measured beat note signal by a probe laser at 1541 nm for different pump laser frequencies. The comb is self-locked in the shaded region between the two lines. The locking range shift with laser frequency shift, demonstrating the self-locked comb works for various f_{rep} . **b** Relationship between the two boundaries of the locking range and the modulation power. **c** Relationship between the microwave amplitude and the locking range, which is well fitted by a linear function.

exceeds 500 kHz for most laser frequencies, with the largest range reaching 550 kHz.

In addition to the optical tuning method, the microwave energy can heat the chip, thus changing the FSR of the microresonator via the thermal effect. This alteration impacts the f_{rep} of the locked state. Figure 4b illustrates how the two boundaries of the locking range shift when the microwave modulation power is adjusted from 21 dBm to 30 dBm, showing that the f_{rep} of the locked state can vary within a range of 8 MHz. From the data in Fig. 4b, we also analyzed the relationship between the width of the locking range and the modulation power. Since the comb line amplitude is proportional to the microwave amplitude of the EO modulation²², and according to the Adler equation for injection locking³⁸, the locking range is proportional to the injection laser amplitude. Therefore, the locking range is proportional to the microwave amplitude, meaning a larger microwave amplitude results in a wider locking range. As depicted in the Fig. 4c, the locking range exhibits a positive relationship with the square root of microwave power (i.e., microwave amplitude), fitting well to a linear function.

Discussion

In conclusion, we have demonstrated the generation of a broadband REO microcomb in a single LN microresonator, achieving a spectral width exceeding 300 nm and more than 1400 comb lines at a 26.03 GHz repetition rate. By utilizing the cooperation between Kerr, Raman and EO nonlinearities, we have addressed the spectral width and noise limitation imposed by Raman scattering, transforming it into a beneficial nonlinear process that enhances the width and the flatness of the optical spectrum. The resulting microcomb is not only broadband but also tunable, supporting on-chip f_{rep} modulation with a tuning range of approximately 550 kHz via self-locking and up to 8 MHz through microwave-induced thermal tuning. These characteristics make it an indispensable tool in applications ranging from high-resolution spectroscopy to advanced telecommunications and quantum information processing. Notably, while anomalous dispersion and Kerr nonlinearity facilitate comb broadening in our system, neither

constitutes a fundamental requirement for the self-locking mechanism. Supplementary studies reveal that normal-dispersion microresonators can achieve limited synchronization. Due to the diminished dispersion-assisted broadening, the spectral width becomes constrained, accompanied by an unobservable locking range. To further improve the spectral width, comb power and tunability of this microcomb system to enhance its performance and practical applicability, there are some feasible optimization strategies. First, the coupled-resonator structure can be implemented to enhance pump-to-comb conversion efficiency³⁹, and combined with the resonant electrode design to improve microwave energy utilization²⁶, it can improve the comb line power. Second, advanced dispersion and dissipation engineering techniques^{35,40} can be employed to precisely tailor the mode linewidth and spectral alignment of the microresonator to improve the performance of the Raman laser and reduce the detuning of the microwave modulation frequency. Finally, the spectral width can be further extended by exploring higher-order Raman processes in engineered microresonators and achieving synchronization of multiple Raman combs through the self-locking scheme. The self-locking mechanism can also be adapted for other parametric and competitive nonlinear processes, such as $\chi^{(2)}$ and $\chi^{(3)}$ parametric oscillation, Brillouin scattering and lasing process. Given the ubiquity of different nonlinearities in integrated nonlinear photonics, our findings may inspire further research into exploiting these interactions to develop novel nonlinear photonic devices.

Methods

Device fabrication

The device is fabricated on a commercial x-cut thin film lithium niobate (TFLN) wafer (NANOLN). The 600-nm-thick TFLN is bonded to a silicon substrate with 500- μm -thick silicon and 2- μm -thick wet oxidation silicon dioxide (SiO_2). Electron-beam lithography is used to define the pattern of the device with hydrogen-silsesquioxane (HSQ) resist. Then, the film is partially etched by argon-ion-based reactive ion etching in an inductively coupled plasma (ICP) etcher to form a 350-nm-depth trapezoidal waveguide cross section with a remaining slab of 250 nm. The whole chip is cleaned by buffered HF solution and RCA1 cleaning solution ($\text{NH}_3:\text{H}_2\text{O}_2:\text{H}_2\text{O} = 1:1:5$) to remove the remaining HSQ resist and the redeposition formed in the etching process. The gold modulation electrodes are patterned using laser direct writing and the metal (15 nm of chromium, 300 nm of gold) is transferred using thermal evaporation and the bilayer lift-off process. The LN racetrack microresonator used in experiments has a top width of 1.4 μm and a sidewall angle of around 60°. The fiber-to-chip coupling loss is approximately 6 dB per facet.

Data availability

All data generated or analyzed during this study are available within the paper. Source data are provided with this paper.

Code availability

The code and the algorithm used in this study are available from the corresponding author upon request.

References

- Kippenberg, T. J., Holzwarth, R. & Diddams, S. A. Microresonator-based optical frequency combs. *Science* **332**, 555 (2011).
- Diddams, S. A., Vahala, K. & Udem, T. Optical frequency combs: coherently uniting the electromagnetic spectrum. *Science* **369**, 267 (2020).
- Liu, J. et al. Emerging material platforms for integrated microcavity photonics. *Sci. China Phys., Mech. Astron.* **65**, 104201 (2022).
- Kippenberg, T. J., Gaeta, A. L., Lipson, M. & Gorodetsky, M. L. Dissipative Kerr solitons in optical microresonators. *Science* **361**, eaan8083 (2018).

5. Gaeta, A. L., Lipson, M. & Kippenberg, T. J. Photonic-chip-based frequency combs. *Nat. Photonics* **13**, 158 (2019).
6. Chang, L., Liu, S. & Bowers, J. E. Integrated optical frequency comb technologies. *Nat. Photonics* **16**, 95 (2022).
7. Spencer, D. T. et al. An optical-frequency synthesizer using integrated photonics. *Nature* **557**, 81 (2018).
8. Liu, J. et al. Photonic microwave generation in the x-and k-band using integrated soliton microcombs. *Nat. Photonics* **14**, 486 (2020).
9. Marin-Palomo, P. et al. Microresonator-based solitons for massively parallel coherent optical communications. *Nature* **546**, 274 (2017).
10. Corcoran, B. et al. Ultra-dense optical data transmission over standard fibre with a single chip source. *Nat. Commun.* **11**, 1 (2020).
11. Wang, B. et al. Towards high-power, high-coherence, integrated photonic mmwave platform with microcavity solitons. *Light. Sci. Appl.* **10**, 4 (2021).
12. Niu, R. et al. khz-precision wavemeter based on reconfigurable microsoliton. *Nat. Commun.* **14**, 1 (2023).
13. Xu, X. et al. 11 TOPS photonic convolutional accelerator for optical neural networks. *Nature* **589**, 44 (2021).
14. Feldmann, J. et al. Parallel convolutional processing using an integrated photonic tensor core. *Nature* **589**, 52 (2021).
15. Diddams, S. A. et al. Direct link between microwave and optical frequencies with a 300 THz femtosecond laser comb. *Phys. Rev. Lett.* **84**, 5102 (2000).
16. Jones, D. J. et al. Carrier-envelope phase control of femtosecond mode-locked lasers and direct optical frequency synthesis. *Science* **288**, 635 (2000).
17. Udem, T., Holzwarth, R. & Hänsch, T. W. Optical frequency metrology. *Nature* **416**, 233 (2002).
18. Shen, B. et al. Integrated turnkey soliton microcombs. *Nature* **582**, 365 (2020).
19. Rowley, M. et al. Self-emergence of robust solitons in a microcavity. *Nature* **608**, 303 (2022).
20. Briles, T. C. et al. Hybrid inp and sin integration of an octave-spanning frequency comb. *APL Photonics* **6**, 026102 (2021).
21. Xiang, C. et al. Laser soliton microcombs heterogeneously integrated on silicon. *Science* **373**, 99 (2021).
22. Zhang, M. et al. Broadband electro-optic frequency comb generation in a lithium niobate microring resonator. *Nature* **568**, 373 (2019).
23. Rueda, A., Sedlmeir, F., Kumari, M., Leuchs, G. & Schwefel, H. G. L. Resonant electro-optic frequency comb. *Nature* **568**, 378 (2019).
24. Yu, M. et al. Integrated femtosecond pulse generator on thin-film lithium niobate. *Nature* **612**, 252 (2022).
25. Cai, J. et al. High-Q integrated lithium tantalate microring resonators for on-chip comb generation. *Opt. Lett.* **49**, 5921 (2024).
26. Zhang, J. et al. Ultrabroadband integrated electro-optic frequency comb in lithium tantalate. *Nature* **637**, 1096 (2025).
27. Schaufele, R. F. & Weber, M. J. Raman scattering by lithium niobate. *Phys. Rev.* **152**, 705 (1966).
28. Leidinger, M., Sturman, B., Buse, K. & Breunig, I. Strong forward-backward asymmetry of stimulated Raman scattering in lithium-niobate-based whispering gallery resonators. *Opt. Lett.* **41**, 2823 (2016).
29. Yang, Q.-F., Yi, X., Yang, K. Y. & Vahala, K. Stokes solitons in optical microcavities. *Nat. Phys.* **13**, 53 (2017).
30. Tan, T. et al. Multispecies and individual gas molecule detection using Stokes solitons in a graphene over-modal microresonator. *Nat. Commun.* **12**, 1 (2021).
31. Li, Z. et al. Ultrashort dissipative Raman solitons in Kerr resonators driven with phase-coherent optical pulses. *Nat. Photonics* **18**, 46 (2024).
32. Li, M. et al. Breaking the efficiency limitations of dissipative Kerr solitons using nonlinear couplers. *Sci. China Phys. Mech. Astron.* **67**, 234211 (2024).
33. He, Y. et al. High-speed tunable microwave-rate soliton microcomb. *Nat. Commun.* **14**, 3467 (2023).
34. Gong, Z. et al. Soliton microcomb generation at 2 μm in z-cut lithium niobate microring resonators. *Opt. Lett.* **44**, 3182 (2019).
35. Gong, Z. et al. Photonic dissipation control for Kerr soliton generation in strongly Raman-active media. *Phys. Rev. Lett.* **125**, 183901 (2020).
36. Wang, C. et al. Lithium tantalate photonic integrated circuits for volume manufacturing. *Nature* **629**, 784 (2024).
37. Herr, T. et al. Universal formation dynamics and noise of Kerr-frequency combs in microresonators. *Nat. Photonics* **6**, 480 (2012).
38. Razavi, B. A study of injection locking and pulling in oscillators. *IEEE J. Solid-State Circuits* **39**, 1415 (2004).
39. Hu, Y. et al. High-efficiency and broadband on-chip electro-optic frequency comb generators. *Nat. Photonics* **16**, 679 (2022).
40. Song, Y., Hu, Y., Zhu, X., Yang, K. & Lončar, M. Octave-spanning Kerr soliton frequency combs in dispersion- and dissipation-engineered lithium niobate microresonators. *Light. Sci. Appl.* **13**, 225 (2024).

Acknowledgements

The authors thank C.-L. Zou for helpful discussions. C.-H.D. is supported by the National Natural Science Foundation of China (12293052), Innovation program for Quantum Science and Technology (2021ZD0303 203), the CAS Project for Young Scientists in Basic Research (YSBR-069), and the USTC Research Funds of the Double First-Class Initiative. C.-H.D. and F.B. are supported by the National Natural Science Foundation of China (92250302). S. W. is supported by the National Natural Science Foundation of China (12293052 and 12104442). M.L. is supported by the National Natural Science Foundation of China (12374361). F.-W.S. is supported by the National Natural Science Foundation of China (62225506). C.-H.D. and S.W. are supported by the Fundamental Research Funds for the Central Universities. This work was partially carried out at the USTC Center for Micro and Nanoscale Research and Fabrication.

Author contributions

S.W., P.-Y.W. and M.L. contribute equally to this work. C.-H.D. and S.W. conceived the experiments, S.W., P.-Y.W., R.M., and F.B. prepared devices, S.W., P.-Y.W. and R.N. built the experimental setup and carried out measurements, with assistance from F.-W.S. and M.L. provided theoretical supports. S.W., M.L., and C.-H.D. wrote the manuscript with input from all co-authors. C.-H.D. and G.-C.G. supervised the project. All authors contributed extensively to the work presented in this paper.

Competing interests

The authors declare no competing interests.

Additional information

Supplementary information The online version contains supplementary material available at <https://doi.org/10.1038/s41467-025-60161-1>.

Correspondence and requests for materials should be addressed to Fang Bo or Chun-Hua Dong.

Peer review information *Nature Communications* thanks Yang Liu, Johann Riemensberger, and the other, anonymous, reviewer(s) for their contribution to the peer review of this work. A peer review file is available.

Reprints and permissions information is available at <http://www.nature.com/reprints>

Publisher's note Springer Nature remains neutral with regard to jurisdictional claims in published maps and institutional affiliations.

Open Access This article is licensed under a Creative Commons Attribution-NonCommercial-NoDerivatives 4.0 International License, which permits any non-commercial use, sharing, distribution and reproduction in any medium or format, as long as you give appropriate credit to the original author(s) and the source, provide a link to the Creative Commons licence, and indicate if you modified the licensed material. You do not have permission under this licence to share adapted material derived from this article or parts of it. The images or other third party material in this article are included in the article's Creative Commons licence, unless indicated otherwise in a credit line to the material. If material is not included in the article's Creative Commons licence and your intended use is not permitted by statutory regulation or exceeds the permitted use, you will need to obtain permission directly from the copyright holder. To view a copy of this licence, visit <http://creativecommons.org/licenses/by-nc-nd/4.0/>.

© The Author(s) 2025